Supplementary Information: Electron tunneling into 2D semiconductors outside the tunnel junction

Yang Xu et.al.

CONTENTS

S1. DEVICE SCHEMATIC AND ADDITIONAL FABRICATION DETAILS

A dual-gate device schematic is used in this study to fully control the carrier density of two graphene (Gr) layers and their band alignment. The additional TMD layer is always placed on top of the top Gr layer with an area smaller than that of the top Gr. This design ensures that the Gr-metal edge contact is defined only in the Gr layer. The stack is prepared with a standard dry transfer method with twist control of two Gr layers. In addition to the method section, the contact temperature between the flakes on the substrate and PC film during stacking for TMD and gate hBN is initially kept at a lower value, e.g., 65°. Then the temperature is increased to 80° or 90° to have a smooth interface for picking up. The edge contact is defined using Ebeam lithography followed by deposition of 10nm Cr/70nm Au at high vacuum between 10^{-7} to 10^{-8} mbar. Two electrodes are defined on each side of graphene layers. This enables measurement of Gr-metal contact resistance on each side. The contact resistance is generally lower than 1 kΩ. A device image of D2 is shown in Fig. 1.

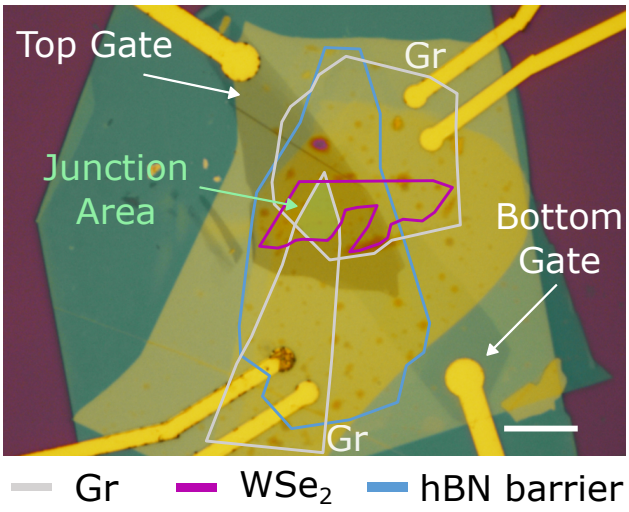

FIG. 1: Optical microscope image of device schematic (D2).

S2. ELECTROSTATIC ANALYSIS

The electrostatic model of the dual-gate device schematic is described through a three-capacitor model (four capacitor plates). Here the top gate graphite and the top graphene form the top gate capacitor C_{TG}. The bottom gate graphite and the bottom graphene

form the bottom gate capacitor C_{BG}. The two graphene electrodes form the capacitor C_{ins} through the insulating tunneling hBN barrier. The chemical potential for the top and bottom graphene layer is μ_T and μ_B as shown in Fig.2a. $\mu_{T,B}$ is larger than 0 when graphene is electron doped, and smaller than 0 when graphene is hole doped. The corresponding carrier density of graphene is defined as n_T and n_B respectively. μ and n have the same sign when considering the doping polarity, defined as $n_{T,B} = sign(\mu_{T,B})\frac{\mu_{T,B}^2}{\pi\hbar^2 v_F^2}$ where v_F is the Fermi velocity of graphene. The potential difference between the two graphene layers is V_b defined by the bias voltage.

$$e^2 n_B - (\mu_B - \mu_T)C_{ins} + eV_b C_{ins} = 0 \tag{1}$$

$$e^2 n_T - eV_{TG}C_{TG} + \mu_T C_{TG} + (\mu_T - \mu_B)C_{TG} - eV_b C_{ins} = 0 \tag{2}$$

The energy offset between two graphene Dirac point is defined as ϕ. It can be determined through the relation:

$$\mu_B - \mu_T + \phi = V_b \tag{3}$$

The geometric capacitance for the gate and hBN barrier capacitor can be expressed as:

$$C_i = \frac{\epsilon_{hBN}\epsilon_0}{d_{hBNi}} \tag{4}$$

where $i = ins, TG, BG$ separately. d_{hBNi} stands for the thickness of hBN to form the capacitor structure. The thickness of a monolayer hBN is 0.33 nm.

Based on the electrostatic analysis, the three parameters: chemical potential of the two graphene layers μ_T, μ_B and Dirac point distance between the two graphene ϕ can be fully determined when applying the three voltages: gate voltages V_{TG}, V_{BG} and the bias voltage V_B, as shown in Fig.2b. From this set of equations, it is understood that the energy offset between the two graphene Dirac point ϕ is generally smaller than the bias voltage V_B.

S3. ANALYTICAL ANALYSIS OF $Gr/hBN/Gr$ TRANSPORT CURRENT

The tunneling current in a Gr/hBN/Gr vertical tunnel junction can be calculated through the expression [1]:

$$I = e\frac{g_s g_v}{2\pi^2\hbar^3}\sum\iint |T_{el}|^2 \frac{\gamma}{(s_B v_F |\mathbf{k} - \hbar\Delta\mathbf{K}| - s_T v_F |\mathbf{k}| + \phi)^2 + \gamma^2} \times (f_B(E) - f_T(E))dk_x dk_y \tag{5}$$

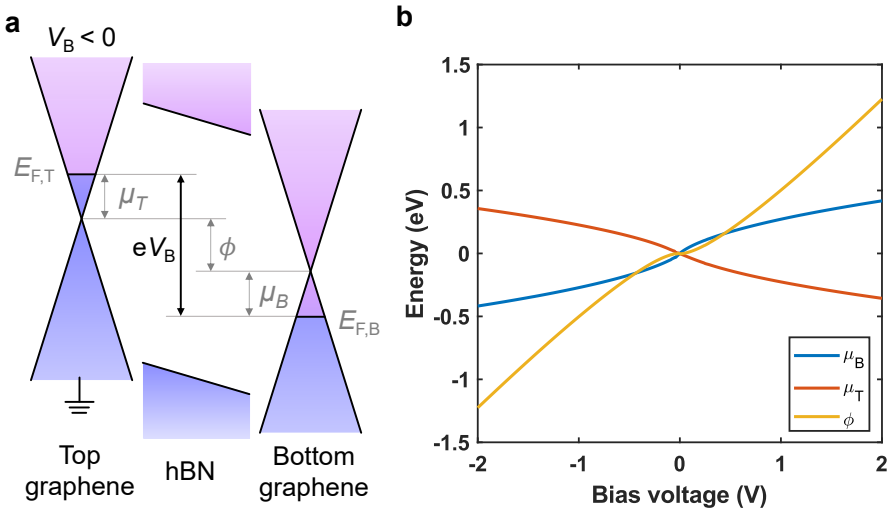

FIG. 2: (a)Schematic of band alignment in a Gr/hBN/Gr device. (b)Calculated parameters of Gr Fermi level/chemical potential and band offset when both gates fixed at zero.

Here T_{el} is the interlayer electron tunneling rate. g_s and g_v describe the electron spin and valley degeneracy. e is the elementary charge. $f_{T,B}$ is the electron Fermi-Dirac distribution function in the top or bottom graphene layer with respect to the corresponding graphene Fermi energy $E_{F,T}$ and $E_{F,B}$. $k = (k_x, k_y)$ is the in-plane momentum of electrons. $s_T, s_B = \pm 1$ are the band indices. γ is related to the inverse electron lifetime, accounting for the quasi-particle state energy broadening. $\epsilon(\mathbf{k}) = \hbar v_F |\mathbf{k}|$ is the graphene electron energy-momentum dispersion. $\mathbf{k_B} - \mathbf{k_T} = \hbar \Delta \mathbf{K}$, where $\mathbf{k_B}$ and $\mathbf{k_B}$ are the in-plane momentum of top and bottom graphene electrons. Calculated conductance map using the tunneling current model is shown in Fig.3. Notice that later in the text in the first-principle transport calculation, only the top gate is used for simplification of the analysis. Besides, in that part of the discussion, definitions of the doping and Fermi energy in graphene are also different when defining the position of the zero potential.

S4. ADDITIONAL TRANSPORT MEASUREMENT

All differential conductance maps are derived directly from the first derivative of the raw data of gate-dependent I-V measurements in the main text and SI except for device D1. Tunneling current in device D1 is around 10 pA at a bias of 1 V and more noisy so that Savgol filter is used to smooth the I-V data first. All tunneling transport measurements

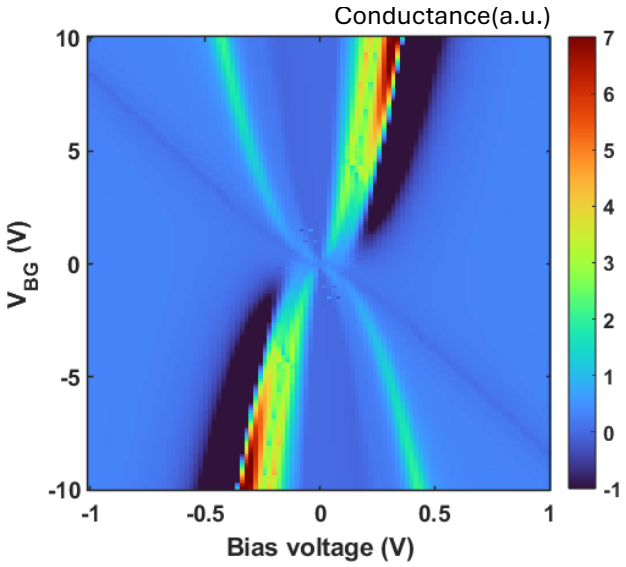

FIG. 3: Calculated conductance (dI/dV) of Gr/hBN/Gr junction based on the tunneling current and electrostatic model. Gate-tunable NDC features are clearly visible.

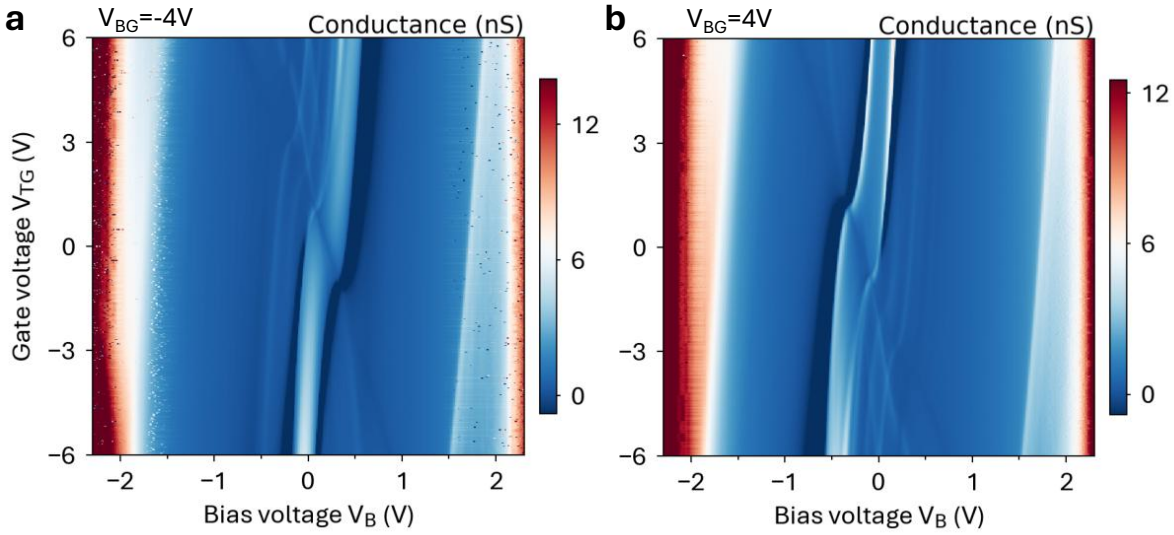

FIG. 4: Experimental gate-dependent differential conductance map obtained for a dual-gated WSe_2/Gr/hBN(3.3nm)/Gr device (D2) where both gates are tuned. Bottom gate is fixed to −4 V (a) and 4 V (b) separately while the top gate is swept from −6 V to 6 V

shown here are measured at 9 K. Besides, Gr Dirac point is assumed to be within $MoSe_2$ and WSe_2 band gap [2].

A. Transport measurement of WSe_2/Gr/hBN/Gr device (D2) with both gates

Here the influence of the bottom gate on the conductance features is investigated in device D2 as described in the main text. The Gr/hBN/Gr tunneling features are prominently influenced by the tuning of the bottom gate as shown in Fig.4. For example, the NDC region with positive bias at zero top gate voltage shifts from a bias of 0.5 V to 0 V while changing the bottom gate voltage from −4 V to 4 V. This is due to low electronic density of state of Gr near Dirac point. However, differential conductance peaks around −1.75 V and around 1.75 V shift less than 0.1 V. This is due to prominent increase of density of state of graphene at a large applied bias of 1.75 V.

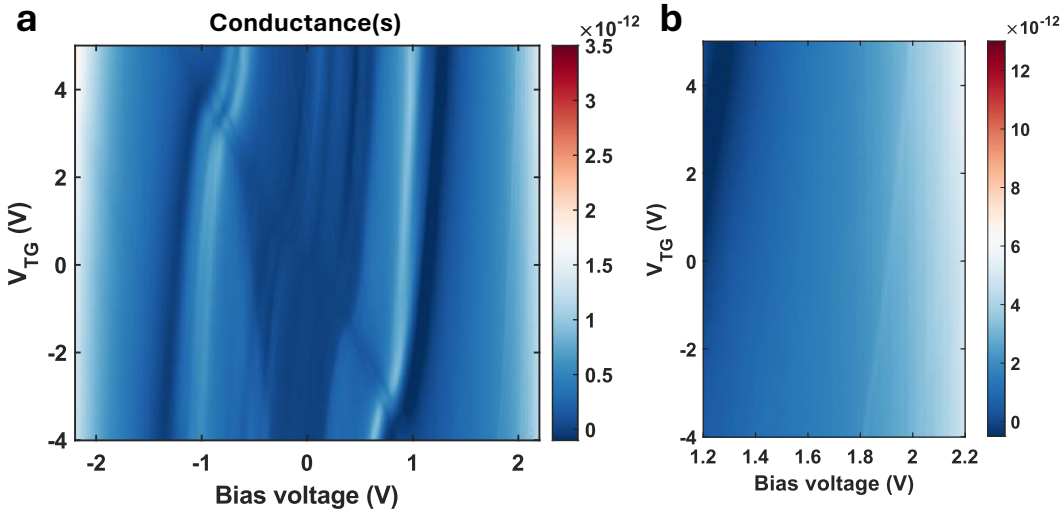

FIG. 5: (a) Experimental gate-dependent differential conductance map obtained for a dual-gated WSe_2/1L hBN/Gr/hBN(3.3nm)/Gr device (D5) with bias voltage ranging from −2.2 V to 2.2 V and top gate ranging from −4 V to 5 V, bottom gate is fixed to zero. (b) Zoom-in of (a) with bias ranging from 1.2 V to 2.2 V to resolve the conductance features.

B. Transport measurement of WSe_2/1L hBN/Gr/hBN/Gr device (D5)

A device (D5) with additional monolayer hBN inserted between the top Gr and WSe_2 is studied. Here WSe_2 and monolayer hBN are fully above the top Gr in the tunneling area similar to area 1 in device D4, while the equivalence of area 2 in Device D4 is absent. This is done to further decouple the Gr and WSe_2 layers with a monolayer hBN. Similar tunneling

transport measurements are performed as shown in Fig.5a. A conductance feature can be observed at the bias of 1.9 V at zero gate voltage, clearly visible in the zoomed-in map depicted in Fig.5b as well. This suggests the existence of an electronic link between top Gr and WSe_2 even separated by a monolayer hBN. At the same time, the peak position shifts to a large bias compared to the bias of 1.75 V in D2. This is probably due to the depinning of the Fermi level between top Gr and WSe_2 when a atomic barrier is inserted.

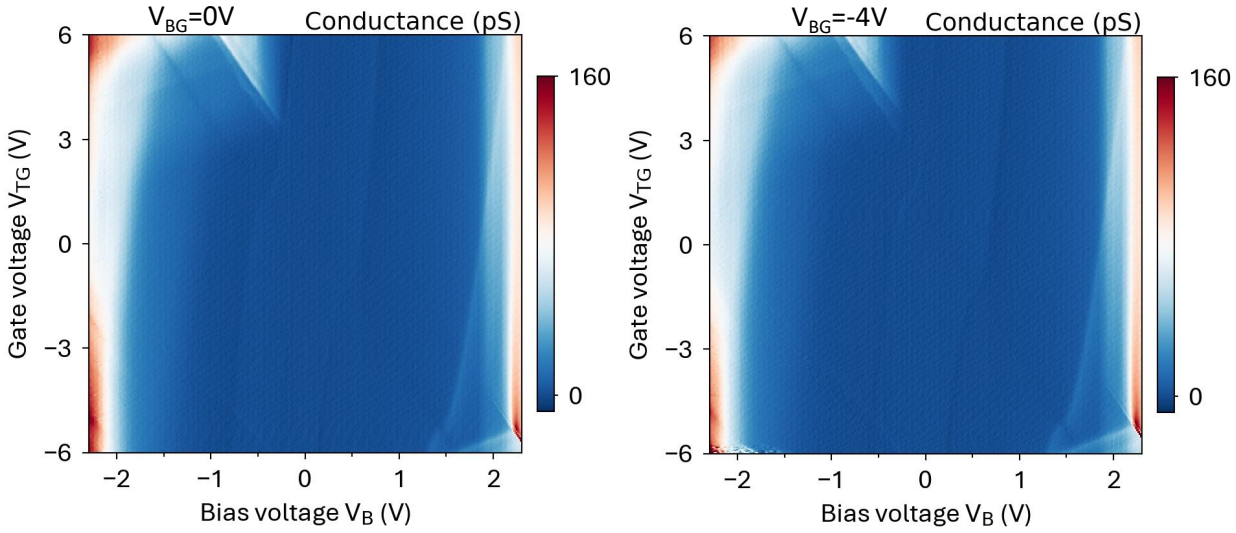

FIG. 6: Experimental gate-dependent differential conductance map obtained for a dual-gated $MoSe_2$/Gr/hBN(3.6 nm)/Gr device (D6) with twist angle of 1° under zero bottom gate voltage in (a) and under −4 V bottom gate voltage in (b).

C. Transport measurement of $MoSe_2$/Gr/hBN/Gr device (D6)

Here a device of $MoSe_2$/Gr/hBN/Gr structure (D6) is studied for the comparison of device D2 with the WSe_2 layer. Gate-dependent differential conductance map derived from the I-V data is shown in Fig.6a when $V_{BG} = 0$. The NDC features from Gr/hBN/Gr tunneling are still visible despite the low tunneling current intensity. In addition, differential conductance peaks are observed at around 1.9 V under zero gate voltage. This peak shifts from 1.4 V to 2.1 V while tuning the top gate from −6 V to 6 V. The relative bias position of 1.9 V in D6 compared to 1.75 V in D2 reflects the lower valence band edge of $MoSe_2$ relative to WSe_2 at the Γ point. Besides, at a bias of −1 V with V_{TG} around −3 V, the sharp lines in conductance

can be observed and originates from defect-mediated tunneling. Finally, similar to the dual-gate dependence in D2, bottom gate can tune the NDC features prominently as shown in Fig. 6b, while the conductance features at 1.9 V stay not obviously tunable. Overall, these measurements suggest the consistency of tunnel injection phenomena in junctions incorporating another TMD material-$MoSe_2$.

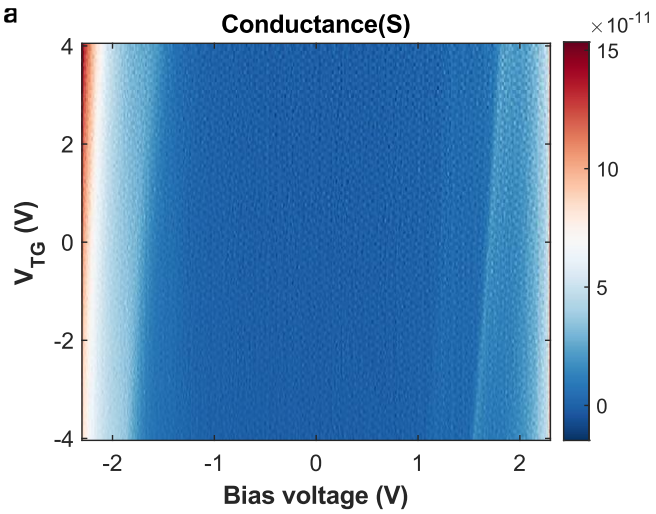

FIG. 7: Experimental gate-dependent differential conductance map obtained for a WSe_2/Gr/hBN/Gr device (D7). Twist angle of graphene is around 14°. Prominent differential conductance peaks can be observed at around −1.72 V and around 1.72 V at zero gate voltage.

D. Transport measurement of WSe_2/Gr/hBN/Gr device with misaligned Gr (D7)

A device (D7) consisting of WSe_2/Gr/hBN/Gr structure with two Gr layers misaligned (14°) is measured to study the influence of the tunneling electron momentum. This large twist angle ensures that the Gr/hBN/Gr elastic tunneling is largely suppressed. No NDC features are observed at small bias as shown in Fig.7. However, conductance features are still observed at 1.72 eV with similar gate-tunable trend compared to the Gr-aligned device D2. Experimentally, the existence of the conductance features in both aligned and misaligned devices indicate that the electron momentum of Gr/hBN/Gr tunnel junction does not prominently influence the observed conductance features. Since bright excitons in monolayer TMDs originate from a direct bandgap with negligible momentum mismatch,

such misaligned condition is not favor of generating bright excitons. This further supports the nature of tunneling into TMD layers outside the junction as proposed in the main text.

E. Transport measurement of WSe_2/Gr/hBN/Gr device with thin hBN (D3)

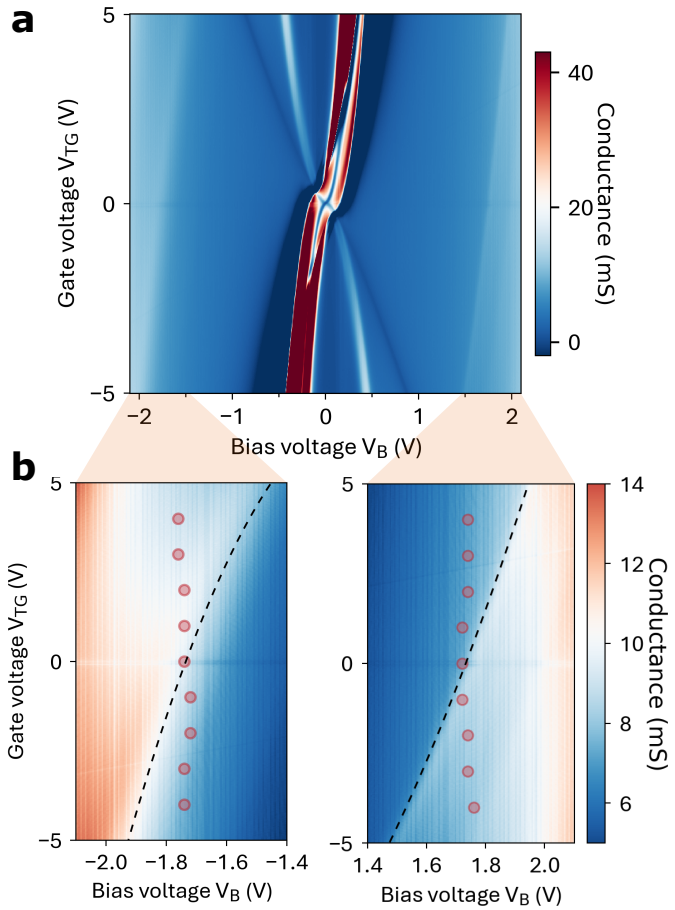

FIG. 8: Experimental gate-dependent differential conductance map obtained for a WSe_2/Gr/hBN/Gr device (D3) with thin hBN barrier of 3 nm in (a) and zoom-in of positive and negative bias voltages in (b).

The full characterization of gate-dependent conductance map of D3 is shown in Fig. 9.

S5. ADDITIONAL OPTICAL MEASUREMENT

A. Additional EL spectra in device D3 and D4

Additional measured negative bias-dependent EL spectra are shown in Fig.9a and gate-dependent EL spectra with a bias of 1.79 V are shown in Fig.9b. Exciton features in the line-cut of the EL spectra in D4 help to identify dark excitons and trions as shown in Fig. 10a,b,c [3, 4]. Besides, the unexpected existence of EL in area 2 of device D4 already proves that there is a close electronic loop to enable charge injection into TMD.(The TMD in area 2 does not directly contact the source, and there is no Gr electrode) This phenomenon is also reproduced in another device (D8) with a structures similar to that of D4 with two junction areas and a monolayer hBN spacer.

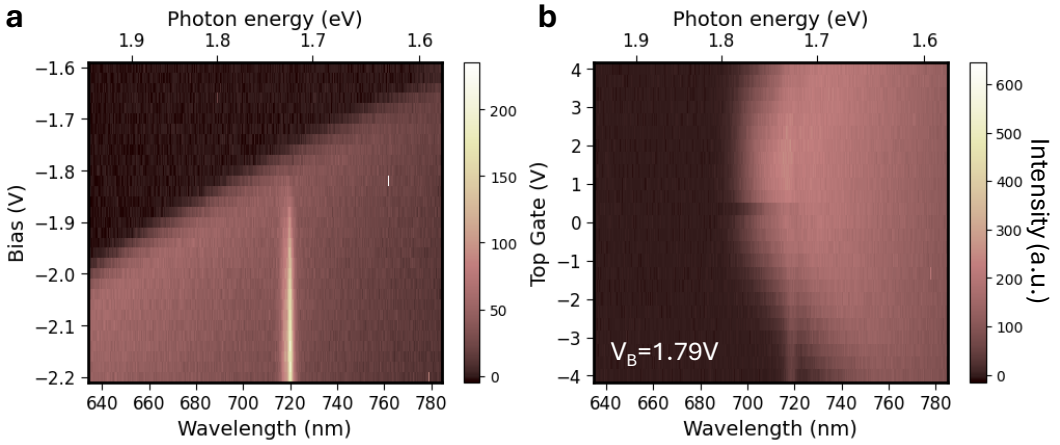

FIG. 9: (a) Measured negative bias-dependent EL spectra with all gate voltages fixed at 0V in D3. (b) Measured gate-dependent EL spectra when bias fixed to 1.79 V.

symmetric gate dependence measures Recognization of dark exciton features in WSe2, single curve

S6. FIRST-PRINCIPLES TRANSPORT CALCULATIONS

To gain insights into the tunneling mechanisms at play, we compute quantum transport properties from first principles. We first perform density functional theory (DFT) calculations. From the equilibrium DFT electronic structure we then compute non-equilibrium properties, using a matrix Green's function approach. Here we describe the procedure for

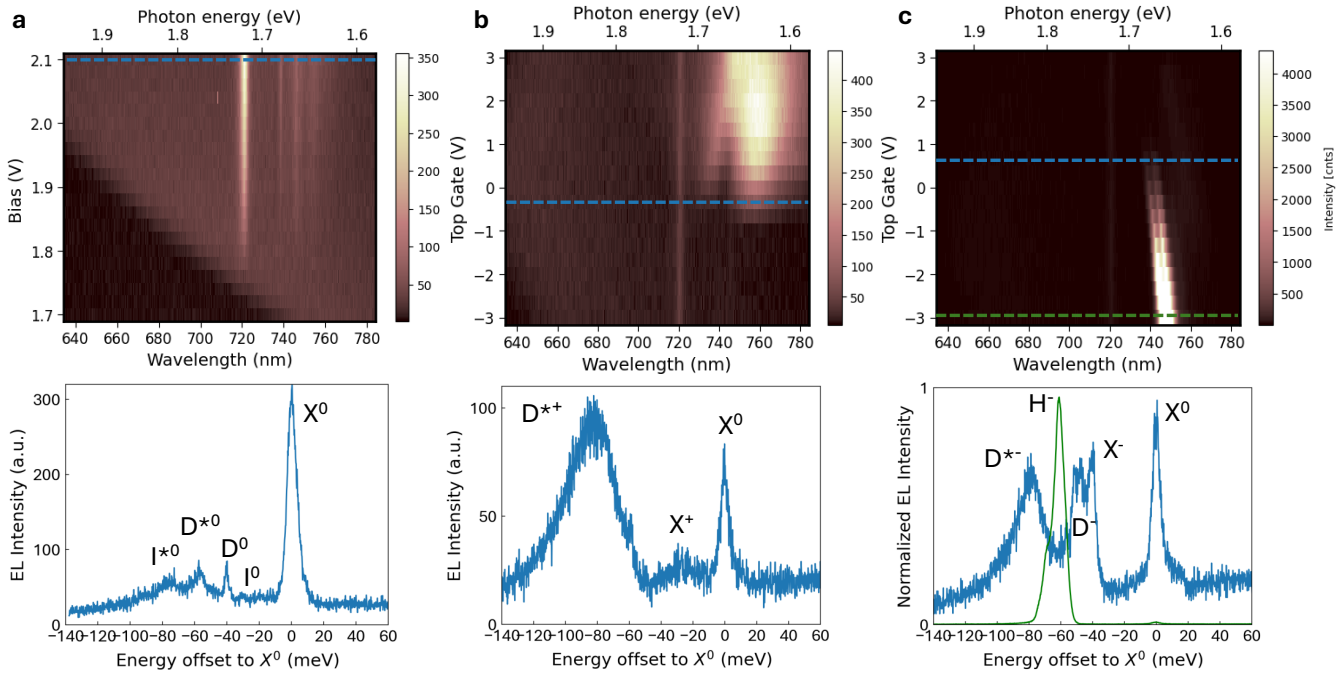

FIG. 10: Line-cut curve in bias and gate-dependent EL spectra in D4 to recognize dark exciton (a), positively charged trion (b) and negative charged trion (c).

obtaining the DFT inputs to the quantum transport calculations, as well as the employed transport formalism.

A. Electronic Structure Calculations

Before assembling the heterostructure cells, we perform cell optimizations on the isolated monolayers of graphene, hexagonal boron nitride (hBN), $MoSe_2$, and WSe_2. From the hBN unit cells we assemble a four-layer, AA'-stacked hBN structure. We then also add graphene layers at either side of the structure in AB-stacking. The resulting strain of **TODO** is placed entirely on the hBN structure. We subsequently perform an ionic relaxation, keeping the cell fixed and including vacuum padding of roughly 35 Å at both ends of the junction. The resulting structure can be seen in Figure 11a.

We finally add monolayers of $MoSe_2$ and WSe_2 on top of this tunnel junction. Using the interface building method implemented in QuantumATK [5, 6], we find a supercell that induces minimal strain, while not making a DFT calculation computationally prohibitive. For both TMDs we have to accommodate mean absolute strain of only $\sim$0.2 %. The resulting

supercells have areas of about 68 Å^2 and have 177 constituent atoms each.

We obtain the electronic structure on k-point grids of $9 \times 9 \times 1$ ($25 \times 25 \times 1$ for the structure without TMD). We finally obtain the Kohn-Sham Hamiltonian and the orbital overlap matrix in an LCAO basis and tight-binding picture, which allows us to efficiently sample the Brillouin during transport.

$$H_{ij} = \langle j|\hat{H}|i\rangle$$

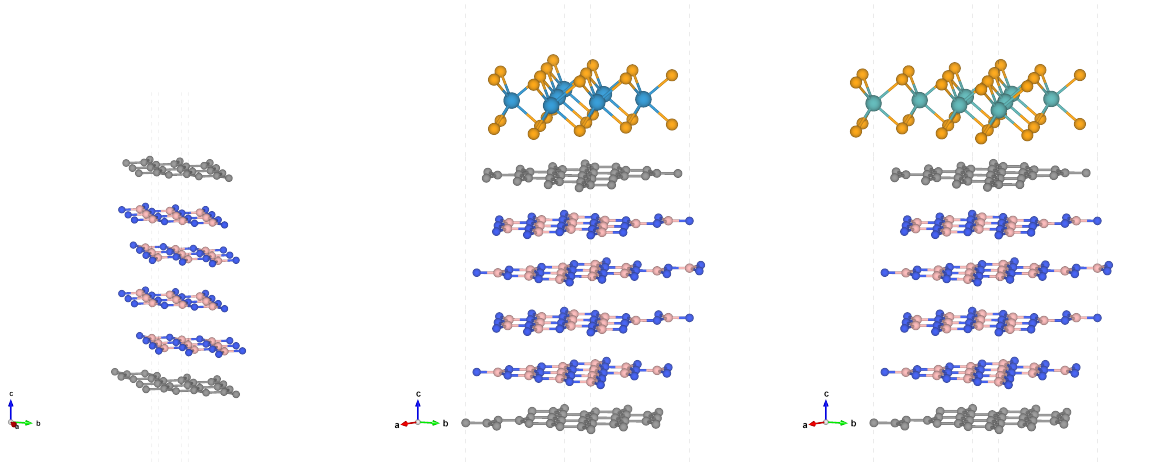

(a) notmd (b) wse2 (c) mose2

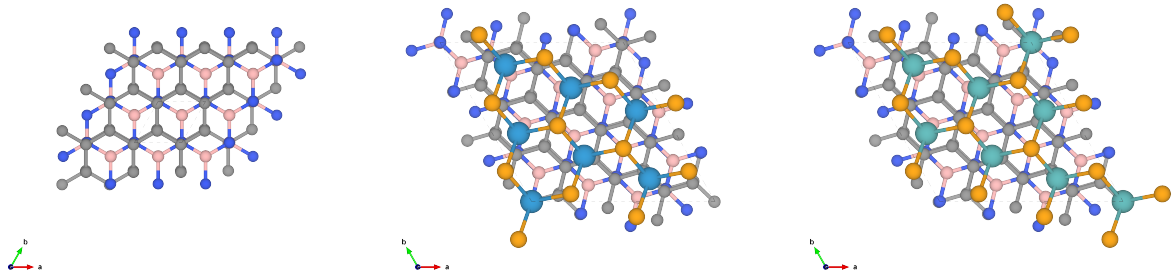

(d) notmd top (e) wse2 top (f) mose2 top

$$\mathbf{H}(\mathbf{k}) = \sum_{\mathbf{R}} \mathbf{H}(\mathbf{R}) e^{2\pi i\, \mathbf{k}\cdot\mathbf{R}}$$

$$\mathbf{S}(\mathbf{k}) = \sum_{\mathbf{R}} \mathbf{S}(\mathbf{R}) e^{2\pi i\, \mathbf{k}\cdot\mathbf{R}}$$

B. Quantum Transport Formalism

As usual in DFT+NEGF, the simulation domain is partitioned into left and right contact regions, as well as a central device region. We write the system matrix

$$\mathbf{M}(E,\mathbf{k}) \equiv \varepsilon\mathbf{S}(\mathbf{k}) - \mathbf{H}(\mathbf{k}) = \begin{bmatrix} \mathbf{m}_L & \mathbf{m}_{LC} & 0 \\ \mathbf{m}_{LC}^\dagger & \mathbf{m}_C & \mathbf{m}_{RC}^\dagger \\ 0 & \mathbf{m}_{RC} & \mathbf{m}_R \end{bmatrix}$$

Here L, R, and C indicate left contact, right contact, and central region, respectively. The matrix blocks $\mathbf{m}_{(L/R)C}$ encode the coupling between the leads and the central region. The complex energy $\varepsilon = E + i\eta$ includes a small shift η away from the real energy axis, which helps avoid poles in the central Green's function. The central Green's function is computed as

$$\mathbf{G}_C(E,\mathbf{k}) = \left[\mathbf{M}(E,\mathbf{k}) + \mathbf{V} - \mathbf{\Sigma}_L(E,\mathbf{k}) - \mathbf{\Sigma}_R(E,\mathbf{k})\right]^{-1},$$

where the matrix $\mathbf{V}$ encodes electrostatic potential across the tunnel junction, as shown in Fig.12. The so-called boundary self-energies $\mathbf{\Sigma}_{L/R}$ are computed from the boundary Green's functions $\mathbf{g}_{L/R}$

$$\mathbf{\Sigma}_{L/R} = \mathbf{m}_{(L/R)C}\mathbf{g}_{L/R}\mathbf{m}_{(L/R)C}^\dagger.$$

In usual approaches to NEGF, the boundary Green's functions are those of leads that extend semi-infinitely along the direction of transport. They are then obtained as the solution to a recursion relation that arises from the constraint that the leads should sit at thermodynamic equilibrium.

In the present systems, however, the electrodes have a finite extent along the transport direction (e. g. a single layer of graphene). We thus employ the finite-dimensional electrode approximation described in [7]. In this approximation, the computation of the boundary Green's function reduces to an inversion of the contact blocks of the system matrix

$$\mathbf{g}_{L/R} = \mathbf{m}_{L/R}^{-1}$$

We can check the validity of this approximation by ensuring that the spectrum of the isolated contact matrices is approximately a subset of the full electronic structure. In other words, the coupling between contacts and the device $\mathbf{m}_{(L/R)C}$ must have a negligible effect on the electronic structure.

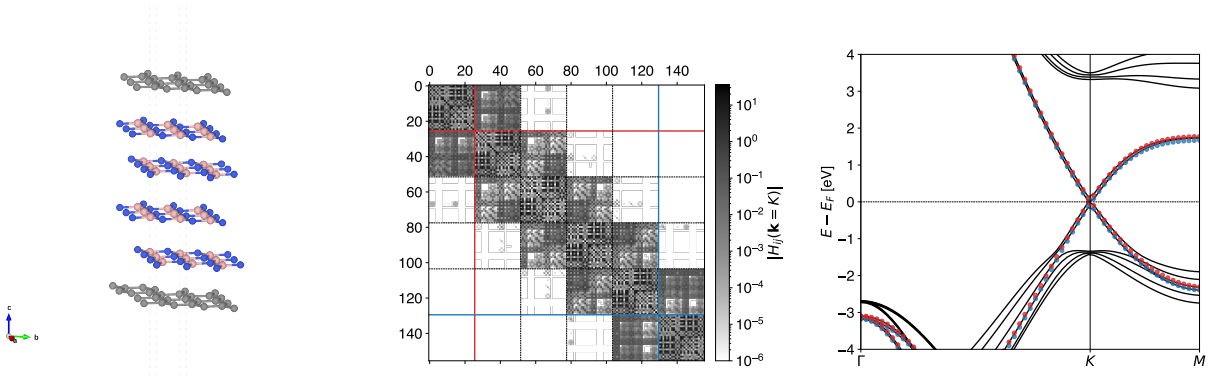

FIG. 12: Device lattice architecture (left), calculated Hamiltonian matrix distribution (middle) and the full contact band structure (right).

We can then continue by computing the contact broadening matrices

$$\mathbf{\Gamma}_{L/R} = i\left(\mathbf{\Sigma}_{L/R} - \mathbf{\Sigma}_{L/R}^{\dagger}\right)$$

from which we get the transmission function

$$T(E, V_b) = \int \mathrm{tr}\left[\mathbf{\Gamma}_L \mathbf{G}_C \mathbf{\Gamma}_R \mathbf{G}_C^{\dagger}\right] \, d\mathbf{k}$$

and finally, the Landauer-Büttiker current

$$J(V_b) = \frac{2e}{h}\frac{1}{A}\int T(E, V_b)\left[f(E-\mu_R) - f(E-\mu_L)\right] \, dE.$$

Here e is the elementary charge, h the Planck constant, $f(E)$ is the Fermi-Dirac distribution and $\mu_{L/R}$ are the contact charge neutrality levels.

C. Electrostatic Model and Inclusion of Top Gate

In the present simulation scheme we do not self-consistently solve for the electrostatic potential. We instead approximate the real-space electrostatic potential as a linear potential drop between the two contacts of the tunnel junction. The magnitude ϕ of this drop, as well as the charge neutrality levels $\mu_{L/R}$ are determined using a parallel plate capacitor model of the junction.

We have $\phi = V_b + \mu_L - \mu_R$, where V_b is the applied bias voltage and $C = \varepsilon_0\varepsilon_r/d$ is the capacitance, with ε_0 and ε_r the vacuum and the relative dielectric permittivity, respectively. Lastly, d is the separation between the two plates. The charge on either of the graphene

plates is modeled by assuming a perfectly linear dispersion relation in two dimensions, and by taking a Fermi-Dirac occupancy in the zero-temperature limit. We arrive at the charge density

$$Q(\mu) = \mathrm{sign}(\mu)\frac{e}{\pi}\left(\frac{e\mu}{\hbar v_F}\right)^2.$$

Here $\hbar$ is the reduced Planck constant and v_F the Fermi velocity in graphene, which we computed as 1.02×10^6 m/s from DFT.

To determine the charge neutrality levels we then have to find μ_L and μ_R such that

$$\begin{pmatrix} Q(\mu_L) + (V_b + \mu_L - \mu_R)C \\ Q(\mu_R) - (V_b + \mu_L - \mu_R)C \end{pmatrix} = \begin{pmatrix} 0 \\ 0 \end{pmatrix}$$

In Figure 14 one can observe how the charge neutrality levels then move away from the equilibrium Fermi level with applied bias voltage V_b.

To model the effect of an additional gate contact, we extend the equivalent circuit model with a gate capacitance C_g and a gate potential V_g. We now need to determine μ_L and μ_R, such that

$$\begin{pmatrix} Q(\mu_L) + (V_b + \mu_L - \mu_R)C \\ Q(\mu_R) - (V_b + \mu_L - \mu_R)C - (V_g - \mu_R)C_g \end{pmatrix} = \begin{pmatrix} 0 \\ 0 \end{pmatrix}$$

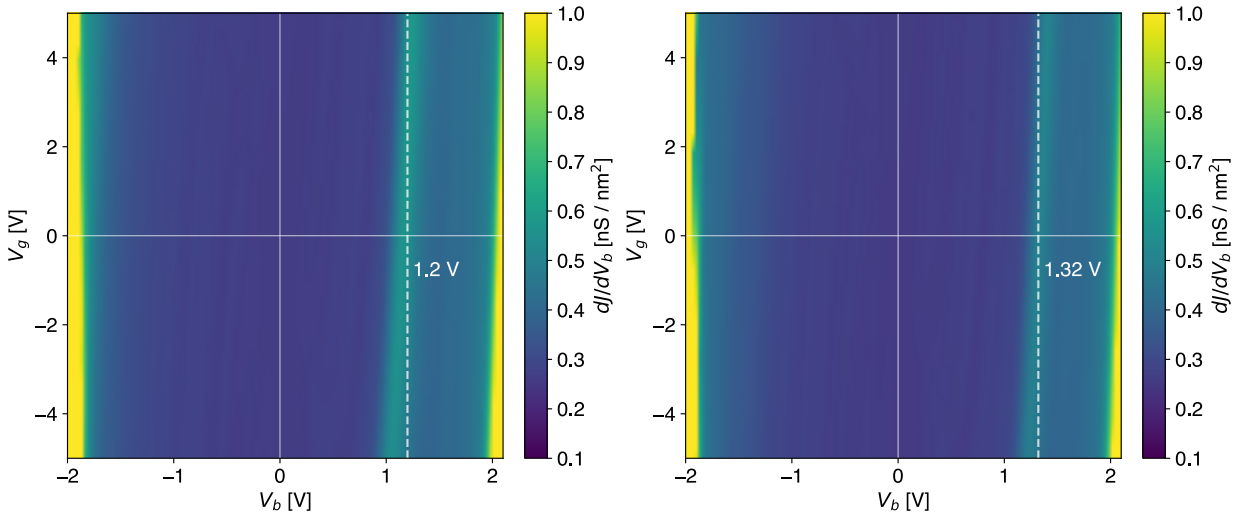

FIG. 13: Calculated top gate-bias dependent conductance map of junctions incorporating WSe_2 and $MoSe_2$.

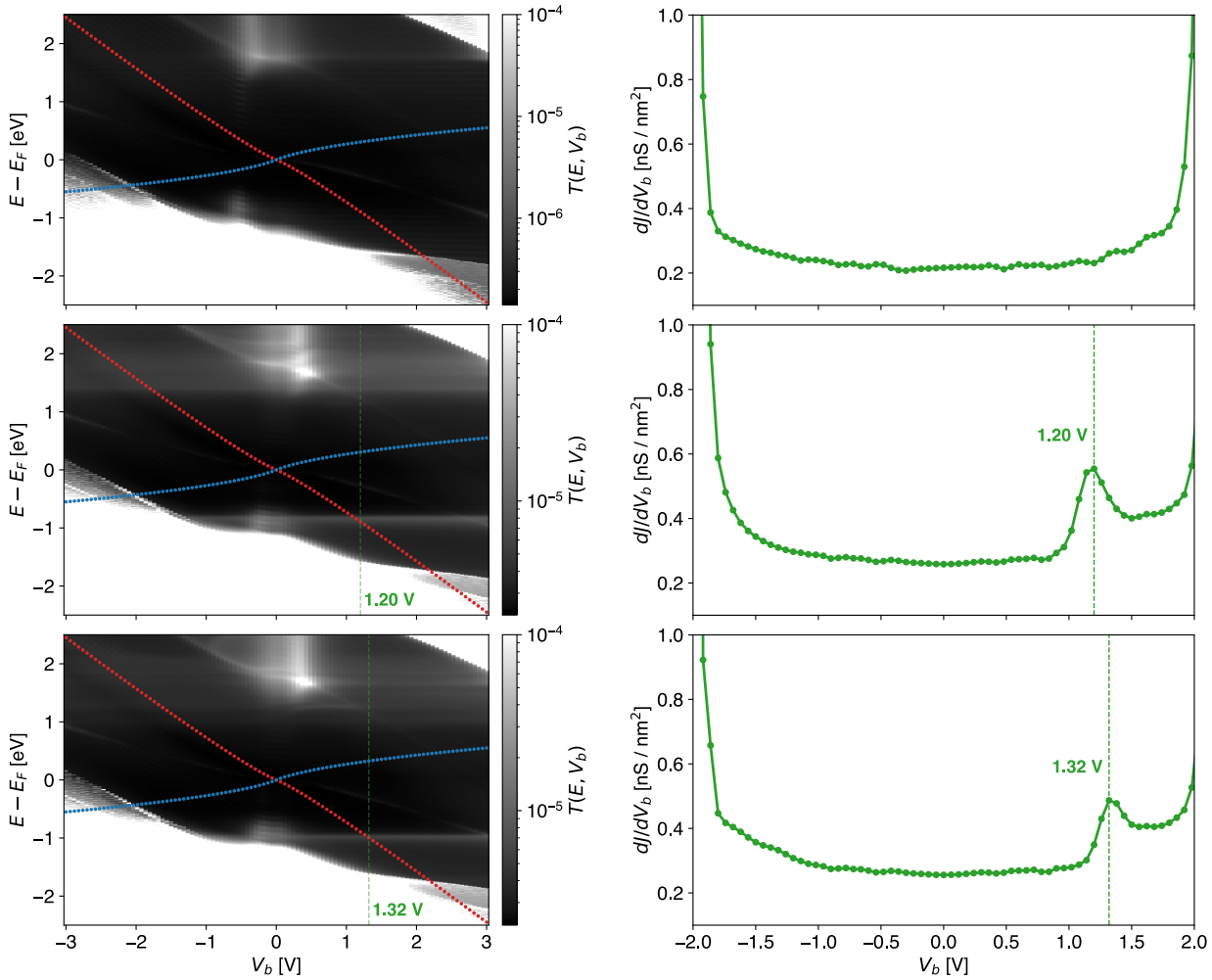

FIG. 14: Tunneling transmission function (left) of the whole tunneling structure including WSe_2 and calculated conductance (right) under three applied bias voltages.

[1] A. Kuzmina, M. Parzefall, P. Back, T. Taniguchi, K. Watanabe, A. Jain, and L. Novotny, "Resonant light emission from graphene/hexagonal boron nitride/graphene tunnel junctions," *Nano Letters*, vol. 21, no. 19, pp. 8332–8339, 2021.

[2] Y. Xu, C. Horn, J. Zhu, Y. Tang, L. Ma, L. Li, S. Liu, K. Watanabe, T. Taniguchi, J. C. Hone, *et al.*, "Creation of moiré bands in a monolayer semiconductor by spatially periodic dielectric screening," *Nature Materials*, vol. 20, no. 5, pp. 645–649, 2021.

[3] M. Yang, L. Ren, C. Robert, D. Van Tuan, L. Lombez, B. Urbaszek, X. Marie, and H. Dery, "Relaxation and darkening of excitonic complexes in electrostatically doped monolayer wse 2:

Roles of exciton-electron and trion-electron interactions," *Physical Review B*, vol. 105, no. 8, p. 085302, 2022.

[4] A. Dijkstra, A. Ben Mhenni, D. Van Tuan, E. Çetiner, M. Schur-Wilkens, J. Kim, L. Steiner, K. Watanabe, T. Taniguchi, M. Barbone, *et al.*, "Ten-valley excitonic complexes in charge-tunable monolayer wse2," *Nature Communications*, vol. 16, no. 1, p. 9743, 2025.

[5] D. Stradi, L. Jelver, S. Smidstrup, and K. Stokbro, "Method for determining optimal supercell representation of interfaces," *Journal of Physics: Condensed Matter*, vol. 29, p. 185901, Mar. 2017. Publisher: IOP Publishing.

[6] S. Smidstrup, T. Markussen, P. Vancraeyveld, J. Wellendorff, J. Schneider, T. Gunst, B. Verstichel, D. Stradi, P. A. Khomyakov, U. G. Vej-Hansen, M.-E. Lee, S. T. Chill, F. Rasmussen, G. Penazzi, F. Corsetti, A. Ojanperä, K. Jensen, M. L. N. Palsgaard, U. Martinez, A. Blom, M. Brandbyge, and K. Stokbro, "QuantumATK: an integrated platform of electronic and atomic-scale modelling tools," *Journal of Physics: Condensed Matter*, vol. 32, p. 015901, Jan. 2020.

[7] T. H. Kim, J. Lee, R.-G. Lee, and Y.-H. Kim, "Gate- versus defect-induced voltage drop and negative differential resistance in vertical graphene heterostructures," *npj Computational Materials*, vol. 8, pp. 1–9, Mar. 2022.